

## Encapsulation of Nanostructures in a Dielectric Matrix Providing Optical Enhancement in Ultrathin Solar Cells

Peer-reviewed author version

Oliveira, Antonio J. N.; DE WILD, Jessica; Oliveira, Kevin; Valenca, Beatriz A.; Teixeira, Jennifer P.; Guerreiro, Joana R. L.; Abalde-Cela, Sara; LOPES, Tomas; Ribeiro, Rodrigo M.; Cunha, Jose M., V; Curado, Marco A.; MONTEIRO, Margarida; Violas, Andre; Silva, Ana Gomes; Prado, Marta; Fernandes, Paulo A.; VERMANG, Bart & Salome, Pedro M. P. (2020) Encapsulation of Nanostructures in a Dielectric Matrix Providing Optical Enhancement in Ultrathin Solar Cells. In: Solar RRL, 4 (11) (Art N° 2000310).

DOI: 10.1002/solr.202000310

Handle: <http://hdl.handle.net/1942/32993>

1 M. Monteiro, Dr. Ana G. Silva  
2 Departamento de Física, Faculdade de Ciências e Tecnologia, Universidade Nova de Lisboa,  
3 Campus de Caparica, 2829-516 Caparica, Portugal  
4  
5

6 Dr. Ana G. Silva  
7 CEFITEC, Departamento de Física, Faculdade de Ciências e Tecnologia, Universidade Nova  
8 de Lisboa, Campus de Caparica, 2829-516 Caparica, Portugal  
9

10 Dr. P. A. Fernandes  
11 CIETI, Departamento de Física, Instituto Superior de Engenharia do Porto, Instituto  
12 Politécnico do Porto, Porto 4200-072, Portugal  
13  
14

15  
16  
17 Keywords: Light management, CIGS solar cells, Gold nanoparticles, Optical enhancement  
18  
19

20  
21 The incorporation of nanostructures in optoelectronic devices for enhancing their optical  
22  
23 performance has been widely studied. However, several problems related with the processing  
24  
25 complexity and the low performance of the nanostructures have hindered such actions in real-  
26  
27 life devices. In this work, we propose a novel way of introducing gold nanoparticles in a solar  
28  
29 cell structure in which the nanostructures are encapsulated with a dielectric layer, shielding  
30  
31 them from high temperatures and harsh growth processing conditions of the remaining device.  
32  
33 Through optical simulations, an enhancement of the effective optical path length of  
34  
35 approximately four times the nominal thickness of the absorber layer was verified with the new  
36  
37 architecture. Furthermore, we demonstrate the proposed concept in a Cu(In,Ga)Se<sub>2</sub> solar cell  
38  
39 device, where the short circuit current density is increased by 17.4 %. The novel structure  
40  
41 presented in this work is achieved by combining a bottom-up chemical approach of depositing  
42  
43 the nanostructures with a top-down photolithographic process, which allows for an electrical  
44  
45 contact.  
46  
47  
48  
49  
50  
51  
52  
53  
54  
55  
56  
57  
58  
59  
60  
61  
62  
63  
64  
65

## 1. Introduction

Solar cells performance firstly depends on an efficient incident light absorption by the active layer.<sup>[1,2]</sup> However, this first requirement may be in conflict with the technologic and economic aim of different photovoltaic technologies to reduce the active layer thickness to several hundreds of nanometers with cost-reduction objectives.<sup>[3-5]</sup> In such cases, unless an effective light management scheme is implemented for total absorption of the incident light, the devices will suffer from vast optical losses.<sup>[6,8]</sup> Interface texturing is a simple and widely implemented light management scheme in the first-generation solar cells architecture, allowing for an efficient light scattering.<sup>[9,10]</sup> However, light texturing needs to be on dimension values close to the wavelength that is intended to manage. While such sub-micrometer texturing is possible in silicon due to its absorber having hundreds of micrometers, for thin films, texturing is not so easy to implement as the roughness ends up being larger than the film thickness itself. Another potential strategy is the implementation of plasmonic metallic nanoparticles (NPs), e.g. silver (Ag) and gold (Au), with several demonstrations of absorption enhancement, but with severe limitations in terms of device implementation.<sup>[7,11-18]</sup> By manipulating the NPs size, shape, spatial arrangement and local environment, its resonance wavelength can be changed.<sup>[19]</sup> Therefore, the scattering and absorption cross-section can be manipulated allowing for a selection of IR wavelength values, which are poorly absorbed by the absorber layer.<sup>[19-23]</sup> For solar cells applications, the absorbed light in the metallic NPs will not contribute to the photocurrent. Hence, the challenge for the photovoltaic technology goes on maximizing the scattering cross-section rather than the absorption one. In order to mitigate the metallic NPs parasitic absorption<sup>[24]</sup>, the NPs are usually placed on the solar cell rear interface improving the scattering as well as the rear reflection.<sup>[24]</sup> Despite being a promising strategy for enhancing the optical path length, the improvements have been limited by the difficulties to integrate the

metallic NPs in the complex and varied architectures adopted by the different technologies.<sup>[25-27]</sup>

Cu(In,Ga)Se<sub>2</sub> (CIGS) solar cells with a typical absorber layer of 2  $\mu\text{m}$  stand out from its commercially available thin film counterparts, presenting the highest light to power conversion efficiency value of all thin film technologies (23.35 %)<sup>[28]</sup> and presenting the photovoltaic technology with the lowest environmental impact.<sup>[29]</sup> Nevertheless, in order to meet economic and sustainable targets, in CIGS based technology, the thickness of the active layer needs to be further decreased.<sup>[29]</sup> Absorption enhancement in CIGS ultra-thin layers has been explored by the implementation of different light management strategies.<sup>[4,8,15,25,30,31]</sup> In this work, we present for the first time an innovative substrate architecture to enhance the optical path length in the CIGS layer: we used Au NPs [diameter of  $(24.6 \pm 3.8)$  nm] aggregates synthesized by a wet chemical process, to create a randomly texturized rear interface. However, it is well known that metal NPs are not thermally compatible with the high temperature deposition process of the CIGS layer.<sup>[30]</sup> Therefore, this issue was addressed by adding an Al<sub>2</sub>O<sub>3</sub> layer that allows for the Au NPs aggregates encapsulation, hence, avoiding their diffusion into the CIGS layer. The addition of a dielectric layer has already been explored in ultra-thin CIGS solar cells, as a way to passivate the rear interface and consequently reduce the rear interface recombination rate.<sup>[32]</sup> Therefore, in this novel rear structure, an attempt to provide an effective encapsulation of the Au NPs aggregates alongside an interface passivation was performed. To evaluate the proposed novel architecture, optical simulations followed by the fabrication and analysis of resulting solar cells were conducted. Optical simulations allowed for accurate descriptions of the optical effects caused by the Au aggregates introduction in the ultra-thin solar cell. We present a deep discussion based on optical simulations and devices results, of how the scattering provided by

NPs aggregates, as well as by the roughness that those aggregates induce on the subsequent layers, influence the solar cells optoelectronic parameters.

## 2. Results and Discussion

In this work, two sets of ultra-thin CIGS solar cells were fabricated and named according to their substrates, as follows:

- i. Ref: sample without nanoparticles nor dielectric;
- ii. NPep: sample where the Au NPs aggregates were deposited between the rear contact (molybdenum) and the  $\text{Al}_2\text{O}_3$  dielectric layer.

After the Au NPs aggregates deposition, sample NPep was submitted to an optical lithographic procedure to develop line patterns on the  $\text{Al}_2\text{O}_3$  dielectric layer (**Figure 1**). Such line pattern will allow for an electrical contact between the rear contact molybdenum (Mo) and the absorber layer CIGS. In sample Ref, the CIGS layer was deposited directly on top of the Mo contact. The final architecture of sample Ref was the following: SLG/Mo/CIGS/CdS/i-ZnO/ZnO:Al.

Whereas, the final architecture of sample NPep was: SLG/Mo/Au NPs aggregates/ $\text{Al}_2\text{O}_3$ /CIGS/CdS/i-ZnO/ZnO:Al. The CIGS was deposited in the same run for both samples with a thickness of  $462 \pm 20$  nm and a Cu/(Ga+In) ratio (CGI) and a Ga/(Ga+In) ratio (GGI) of 0.3 and 0.8, respectively.

### 2.1. Rear structure characterization

The analysis of the Au NPs surface coverage was performed using scanning electron microscope (SEM) top view images. Through the deposition method used in this work, the NPs, with dimensions of  $(24.6 \pm 3.8)$  nm, tend to form aggregates in the Mo substrate, as shown on **Figure 2**, where a representative SEM image of the Mo substrate with deposited Au NPs (sample NPep) before any lithographic step is presented. The determined average surface coverage of these aggregates was  $(4.6 \pm 0.7)$  %.

The relative total reflection of sample NPep after the lithographic procedure, alongside with sample Ref was measured. With the new architecture, there is a slight decrease in the total reflection in comparison to the Ref sample, as shown on **Figure 3 a)**, which might have stem from parasitic absorption derived from the deposited metallic NPs. Despite the poor total reflection, the diffuse reflection can more accurately describe the capability of increasing the optical path length in the absorber layer, since it measures the amount of light scattered away from the specular direction.<sup>[14]</sup> In **Figure 3 b)**, where the relative diffuse reflection of both samples is presented, an increase in this parameter is verified when comparing sample NPep to sample Ref. The increase of the interface irregularity, due to the line fabrication process, might have contributed to the diffuse reflection enhancement. In order to clarify this point, the diffuse reflection of a patterned sample without Au NPs is also represented in Figure 3 b). As it is shown, the diffuse reflection of the patterned sample is lower than sample NPep, suggesting that the presence of rough metallic aggregates significantly contributes to the relative diffuse reflection enhancement of sample NPep over sample Ref. However, when these rear structures are implemented in the solar cell, these results may differ as the light will be incident on the substrate coming from the CIGS layer -and not air as in this case -, therefore the refractive index schematics will be, somehow, different.

After the lithographic procedure to create line contacts, a SEM top view image (**Figure 3 c)**) shows that Au NPs aggregates remain in the contact line (dark lines) after the etching process. The reason why the Au NPs aggregates remain is because the reactive ion etching procedure relies on chlorine ions that create a non-volatile compound when reacting with Au at high temperatures.<sup>[33]</sup> Since the Al<sub>2</sub>O<sub>3</sub> layer was completely etched from the line contacts, then, the Au material is free to diffuse into the CIGS layer due to its high temperature growth. Such diffusion constitutes an issue for the CIGS solar cell performance, since it is known that the

metal diffusion into the CIGS during its growth may degrade the solar cell electrical performance.<sup>[31]</sup>

Atomic force microscopy (AFM) measurements of sample NPep, shown in **Figure 4**, allowed for an accurate measure of the line contact width and pitch (inter-distance between the start of two consecutive lines) values. It is noted from Figure 4 a) and b) that the contact lines are perfectly defined. The line contact width was measured on the top of the Mo layer considering that the 25 nm of Al<sub>2</sub>O<sub>3</sub> were completely etched in the line contact, as it is shown in Figure 4 b). An average line contact width of 991 nm with a standard deviation value of 19 nm was achieved. The average pitch was 2024 nm with a standard deviation value of 13 nm. The low standard deviation of the pitch value demonstrates that it is a uniform feature throughout the whole sample area.

## 2.2. Optical simulations

Optical simulations of the fabricated solar cells were performed through the Finite-Difference Time-Domain (FDTD) solutions package from the *Lumerical* commercial software.<sup>[34]</sup> The surface roughness of the samples with NPs was imported from AFM measurements, this roughness was then translated to the subsequent solar cell layers, assuming a conformal growth over the Au NPs aggregates. The addition of the Au NPs aggregates enhances the light absorbed in the CIGS layer for most of the simulated wavelength region, as it is shown on **Figure 5 a)**, where the CIGS and substrate (Mo/Au NPs/Al<sub>2</sub>O<sub>3</sub>) absorbance, alongside with the simulated short-circuit currents ( $J_{sc}$ ) (assuming no electrical losses), are presented. For wavelength values below 900 nm, a reduction in the total solar cell reflectance is observed, as presented in **Figure 5 b)**. The roughness induced by the aggregates on the layers above the CIGS leads to an improvement of the anti-reflection properties of the solar cell stack. The roughness effect on the decrease of the total solar cell reflectance has already been previously reported.<sup>[35,36]</sup> The

light absorption enhancement for wavelength values above 900 nm for the NPep solar cell might have happened due to two effects: i) a possible improvement of the anti-reflection properties; and ii) an increase in the rear optical diffuse reflection, due to the aggregates and a subsequent reduction of the parasitic rear absorption. The conjugation of these factors leads to a  $J_{sc}$  enhancement of 3.49 mA/cm<sup>2</sup> (abs) over the Ref solar cell. Moreover, by looking at the amount of light that is absorbed in the rear contact – the parasitic absorption shown in Figure 5 a) – we can say that this structure heavily minimizes rear parasitic absorption. To study the influence that the Au NPs aggregates have on the optical path length in the CIGS layer, we followed a method described by Hegedus *et al.*<sup>[37]</sup> From which, we were able to determine a wavelength dependent constant,  $m$ , that quantifies the increase in the optical path length, due to light scattering and optical reflection effects. For that, a CIGS absorption profile must be calculated, assuming full carrier collection and discarding electrical losses. As such, the data given by our optical model was then used, as it accounts for no electrical losses. Followed by the calculation of the CIGS absorption coefficient using the optical data from the simulation,  $m$  can be determined through the use of Equation (1).

$$A_{CIGS} = 1 - e^{[-\alpha(\lambda) \cdot d \cdot m(\lambda)]} \quad (1)$$

with  $A_{CIGS}$  being the absorption in the CIGS layer,  $\alpha$  the absorption coefficient and  $d$  the CIGS thickness. In essence,  $m$  is a parameter that for each wavelength value quantifies how much light is absorbed in a light trapping structure in reference with an absorber of equal thickness without any light trapping, hence  $m$  can be called light-path extension. In the Ref device, the light-path extension increases throughout the simulated wavelength region until reaching a maximum of 1.3 (arb. units), as shown on **Figure 5 c)**, where the dependence of the calculated  $m$  on the wavelength is shown for the Ref and NPep devices. Therefore, even the standard CIGS



57 solar cell architecture already has some light trapping schemes that work, mostly due to some

58  
59  
60  
61  
62  
63  
64  
65

of Mo reflection. We note that the light-path extension starts with values close to zero and increases reaching a value of 1 at 900 nm. Such increase of the light-path extension means that for wavelength values in which  $m < 1$ , the CIGS thickness required to fully absorb the incident light is smaller than the thickness of the absorbers used in this study. To support this claim, **Figure 5 d)**, shows the absorption length of CIGS, with a GGI of 0.31. As it is shown in Figure 5 d), in the 300 to 900 nm wavelength region the thickness needed to absorb most of the incoming photons is lower than 500 nm, hence  $m < 1$ . For wavelength values above 900 nm, the needed thickness to absorb most of the incoming light is larger than the absorber physical thickness. The increase in the optical path length ( $m > 1$ ) in the Ref device for wavelength values above 900 nm, may then be attributed to the increase on the rear optical reflection by the rear contact, Mo. Despite its poor optical reflectivity and parasitic absorption problems, Mo is still able to enhance the optical properties of ultra-thin CIGS devices. With the addition of the Au NPs aggregates (NPep device), the optical path length increase is higher than in the Ref device over all the simulated wavelength region, as presented on Figure 5 c). For wavelength values below 900 nm, as opposed to the Ref device, the light-path extension reaches values higher than 1, such increase is related to the anti-reflection improvement of the solar cell stack surface, as in this regime the thickness is enough to fully absorb incoming light. Furthermore, in the IR wavelength region, the light-path extension reaches a maximum of 4.3 at 1030 nm.

As discussed before, the optical path length increase might be related to the improvement of the rear interface scattering, due to the presence of Au NPs aggregates. The performed optical simulations demonstrate that the introduction of the Au NPs aggregates in the solar cell can lead to a  $J_{sc}$  increase of 3.49 mA/cm<sup>2</sup> and an enhancement in the optical light-path extension 4 times the nominal thickness of the absorber. Although these simulations show the positive influence of the Au NPs aggregates on the ultra-thin CIGS solar cells optical properties, they

only account for optical losses. Hence, the influence of Au NPs aggregates on the above layer must be experimentally tested.

### 2.3. Solar cell characterization

An X-ray photoelectron spectroscopy (XPS) analysis was conducted on NPep solar cell to verify if the encapsulated Au in the dielectric matrix was still present after the harsh CIGS growth. For this purpose, depth profile studies of the atomic percentage of the CIGS elements, aluminum (Al), oxygen (O), gold (Au) and molybdenum (Mo), from the middle of the CIGS layer until the rear contact, were done (**Figure 6 a**). Through the analysis of Figure 6 a), one verifies that Au starts being detected prior to O and Al suggesting that some Au diffused into the CIGS layer. The Au contribution, prior to the detection of O and Al is very low and in agreement with some NPs being unetched in the line contacts being able to diffuse into the CIGS. However, the signal of the Au atomic percentage follows the same tendency as the atomic percentages of Al and O, suggesting that most gold is encapsulated. In **Figure 6 b**), two different etching depths (A: 461 nm; B: 470 nm) are represented in a schematic of the studied structure. The XPS spectra of O 1s, Al 2s and Au 4f on two different etching depths (A and B) are represented on **Figure 6 c**). It is important to notice that the peak at 116 eV (Kinetic Energy ~1370 eV) in the Al spectrum was attributed to a Se auger, since it appears throughout etching depths corresponding to the CIGS layer and it is in line with the kinetic energies determined in [38]. As it is shown in Figure 6 b), at point A, only 4 nm outside the first Al and O detections, it is possible to observe the Au 4f core-levels, whereas the O 1s and Al 2s peaks cannot be properly quantified at this depth, further demonstrating some Au diffusion to the CIGS layer. Nonetheless, at a higher etch depth (point B), where the O 1s (532.1 eV) and the Al 2s (120.2 eV) peaks can be deconvoluted, the intensity of the Au peaks is relatively higher than the intensity at point B, suggesting once again that most Au is encapsulated with the Al<sub>2</sub>O<sub>3</sub> layer.

The XPS analysis suggests that the small amounts of Au that diffused into the CIGS layer may have been the ones present on the line contacts (Figure 3 c)), whereas the Au inside the  $\text{Al}_2\text{O}_3$  remained effectively encapsulated, confirming the effectiveness of the 25 nm dielectric matrix of avoiding Au diffusion into the CIGS layer.

The current density vs voltage (J-V) illuminated and dark curves of Ref and NPep solar cells were measured and are presented on **Figure 7 a)**, with the values of the figures of merit extracted from the curves summarized in **Table 1**, where the  $J_{sc}$  values, obtained from the external quantum efficiency (EQE) spectra (see **Figure 7 b)**), are additionally shown. From the J-V curves analysis, it is clear that both devices show evidences of shunting, a typical situation of ultrathin devices, where the reduced thickness facilitates pin-holes.<sup>[31]</sup> In order to understand the impact of the Au aggregates in the CIGS solar cell optoelectronic properties, the obtained figures of merit values for this device were compared to those of Ref device. Lower open circuit voltage ( $V_{oc}$ ) and fill factor ( $FF$ ) values were obtained for NPep device with respect to the Ref device. The lower performance of these electrical parameters indicates that the integration of the Au NPs had a detrimental effect on the optoelectronic properties. However, the degradation of the  $V_{oc}$  and  $FF$  was also verified in previous attempts to implement NPs in thin film solar cells.<sup>[26,27]</sup> Nonetheless, it is important to understand the fundamental reasons that led to the deterioration of these two parameters. Firstly, the  $V_{oc}$  depends directly on the CIGS bandgap energy value. A well-established empirical approach based on bandgap extraction using EQE analysis<sup>[39]</sup> was used to estimate this energy value for the two devices (not shown), and a difference of approximately 6 meV was obtained between the two bandgap energy values, which is far from the difference of 58 mV obtained between the  $V_{oc}$  values of the two solar cells. This opens the discussion about the impact of the integration of the Au NPs aggregates on the optical, recombination and parasitic losses. The  $V_{oc}$  is significantly affected by recombination

losses, whereas  $FF$  reflects mainly parasitic ones.<sup>[40]</sup> Hence, the decrease of the  $V_{oc}$  value may be in fact linked to an increase of the interface area inherent to the roughness of the Au NPs aggregates. The roughness may have led to an increase of the rear interface defects density, which would increase the rear interface recombination rate. Additionally, despite the verification that most of the Au is encapsulated with the  $Al_2O_3$  layer through the XPS analysis, the diffusion of the Au left unetched in the line contacts into the CIGS may have led to additional recombinative centers, contributing to a  $V_{oc}$  deficit. From an  $FF$  point of view, the performance of this figure of merit might be limited on the NPep device by the formation of pinholes promoted by the roughness inherent also to the Au NPs aggregates. Figure 7 b) shows a representative EQE spectrum for the two studied devices and a broadband enhancement is observed in the NPep device EQE spectrum comparing to the Ref one, in good agreement with the optical enhancement verified by the performed optical simulations (see Figure 5 a)). The trend observed in EQE is also reflected in the  $J_{sc}$  values, with an increase of  $3.70 \text{ mA/cm}^2$  on the average value (abs) when the NPep device is compared with the Ref device. The  $J_{sc}$  increase surpasses the one observed through optical simulations ( $3.49 \text{ mA/cm}^2$ ). The difference between both values demonstrates that besides the optical enhancement, there is also an improvement of the optoelectronic properties of the device through the implementation of the novel architecture, since the performed simulations only account for optical effects. At lower wavelength values, the observed lower optical reflection in the NPep device, shown in Figure 7 b), points out to the improvement of the anti-reflective properties with the introduction of the Au NPs aggregates. Therefore, the obtained EQE enhancement in this wavelength region might have resulted from an improvement of the solar cell anti-reflection properties due to the roughness induced from the conformal growth of the subsequent layers over the Au NPs aggregates. The reduced reflection is, therefore, the main responsible for the EQE enhancement for wavelength values

lower than 900 nm, because in this wavelength range most of the light is absorbed in the CIGS layer without interacting with the Au NPs aggregates. At longer wavelength values ( $> 900$  nm), alongside with the anti-reflection improvement, the observed EQE increase might have also been a result of the extension of the optical path length in the CIGS layer, produced by the scattering provided by the rough metallic aggregates at the rear structure. Similar results were obtained by Morawiec *et al* in <sup>[14]</sup>, where plasmonic Ag NPs also led to a broadband EQE enhancement, but in that case of a n-i-p a-Si:H solar cell.

The increase in the diffuse reflection of the sample with Au NPs aggregates over the reference sample, demonstrated the potential of enhancing the  $J_{sc}$  in solar cell devices with this novel architecture. However, a viable integration of these nanostructures in ultra-thin devices is not as simple as it may look. For example, the reactive ion etching (RIE) procedure utilized was incapable of completely etching the Au material from the line contacts, therefore, the Au material was free to diffuse to the CIGS layer during the absorber's high temperature growth ( $550$  °C). For a proper removal of the NPs inside the line contacts, either an etching process that could remove both  $Al_2O_3$  and Au could be used, or a second etching would be needed. However, due to the increased complexity of both these processes, we decided to proceed with the fabricated sample as a proof-of-concept for the encapsulation of NPs and its introduction in the solar cell structure. After the solar cell fabrication, an XPS analysis was performed on NPep device and we were able to verify the diffusion of Au into the absorber layer, this phenomenon was attributed to the presence of Au in the line contacts after the etching procedure. Nonetheless, the XPS analysis suggested that most Au was encapsulated with the dielectric matrix. The impact of this novel nanostructure on the solar cell's optoelectronic properties was studied through J-V and EQE measurements. The introduction of these rough metallic nanostructures

translated in a broadband EQE increase that corresponded to a 17.4 % improvement of the device  $J_{sc}$ . The verified optical enhancement was attributed mainly to two factors: i) an improvement of the solar cell's anti-reflection properties and ii) the enhanced rear scattering. However, the optical improvement was also accompanied by a drop of the device  $FF$  and  $V_{oc}$ . The  $V_{oc}$  degradation could be caused by either an increase of the rear interface recombination, due to the roughness inherent with the Au NPs aggregates, but also due to the diffusion of Au to the absorber layer during its high temperature growth, which led to additional recombinative centers, contributing to a  $V_{oc}$  decline. The  $FF$  drop was attributed to the possible formation of pinholes, caused by the roughness inherent to the Au NPs aggregates.

### 3. Conclusion

In this work, we demonstrated an optical enhancement through the introduction of encapsulated rough metallic NPs aggregates in solar cell devices. A significant  $J_{sc}$  increase of up to 3.70 mA/cm<sup>2</sup> was achieved in comparison with a reference device. With an XPS analysis, we were able to demonstrate the presence of Au NPs aggregates encapsulated in 25 nm dielectric layer after the harsh growth conditions of the absorber layer. Through the combination of the several characterizations presented and the  $J_{sc}$  increase of the device, we can say that the procedure introduced here allows for nanostructures to be encapsulated in a dielectric matrix being able to survive the harsh conditions of CIGS solar cell processing. The obtained results demonstrate the potential to combine a passivation approach to reduce the rear interface recombination with the implementation of plasmonic or photonic nanostructures that can enhance the optoelectronic performance of ultra-thin devices. Improvements on how to mitigate the  $V_{oc}$  and  $FF$  losses are related with an etching procedure that would remove the NPs in the line contacts and better surface passivation techniques for the increased roughness.





## Experimental Section

### *Synthesis of Gold Nanoparticles*

The performed synthesis aimed to produce spherical Au NPs with a nominal diameter of  $(24.6 \pm 3.8)$  nm. The experimental procedure for this synthesis was based on the work of Enüstün *et al.*<sup>[41]</sup> First, a solution of 0.25 mM chloroauric acid ( $\text{HAuCl}_4$ ) in milli-q water (MQ), was brought to boiling for 5-10 min under magnetic stirring. When the temperature reached  $\sim 70^\circ\text{C}$ , 32.7 mL of a warm ( $\sim 50$ - $60^\circ\text{C}$ ) solution of sodium citrate dihydrate ( $\text{C}_6\text{H}_9\text{Na}_3\text{O}_9$ ), 65.3 mM (in MQ) was added. When adding the citrate the yellow coloured solution turned colourless. The final mixture was left under constant temperature and magnetic stirring until it turned to a red wine color indicating the formation of gold particles. The suspension was cooled down until room temperature ( $\sim 22^\circ\text{C}$ ), kept in the dark and stored at  $4^\circ\text{C}$  until further use. The estimated Au concentration (0.12 mM) of the final solution was then measured through the solution absorbance at 400 nm (not shown).<sup>[42]</sup>

### *Deposition of the Au NPs aggregates*

The Au NPs were deposited on top of a Mo layer (350 nm), on a substrate of Soda-Lime Glass (SLG). Prior to the deposition, the Mo layer was functionalized by adsorbing an aqueous solution of 2% Poly(diallyldimethylammonium chloride) (PDPA) for 1 minute followed by 2 minutes of water rinsing and  $\text{N}_2$  drying of the substrate. The self-assembly of nanoparticles was carried out by simply immersing the substrate into a solution of Au NPs (0.12 mM), during 1 hour. The samples were then thoroughly rinsed with MQ and dried with  $\text{N}_2$ .

### *Photolithographic procedure*

A schematic illustration of all the procedures performed on sample NPep prior to the absorber deposition is presented in Figure 1. For the NPs encapsulation, 25 nm of  $\text{Al}_2\text{O}_3$  were deposited

by Radio Frequency (RF) sputtering employing a TIMARIS flexible target module DC/RF Sputter tool. The substrates were then coated with 600 nm of a positive photoresist, AZ1505. Afterwards, the samples were exposed using a Direct Write Laser tool (DWL system, DWL 2000), with a laser wavelength of 405 nm. The nominal pattern design has a trench configuration and its dimensions were based on previous results.<sup>[43]</sup> The samples were developed for 60 seconds using the AZ:400K 1:4 developer. Then, to expose the rear contact, a RIE step was used employing a SPTS-ICP tool, for 45 seconds. The remaining photoresist was removed by immersing the samples in an ultrasound bath with acetone for 30 minutes followed by a 5 minutes bath in deionized water.

#### *Solar cell's fabrication*

Before the CIGS growth, 7 nm of Sodium Fluoride (NaF) were evaporated on the samples. For the CIGS growth, a one stage co-evaporation with a flat profile was used. The substrate temperature during the process was kept at 550 °C. The average CIGS thickness measured by X-ray fluorescence (XRF) was 462 nm with [CGI] = 0.80 and [GGI] = 0.30. The fabrication details for the buffer and window layers can be found elsewhere.<sup>[44]</sup> Thirty-two solar cells with an area of 0.5 cm<sup>2</sup> were mechanically scribed on each sample.

#### *Advanced characterization*

A morphological analysis of the patterned sample was performed through AFM (AFM Dimension Icon system), which was used in tapping mode with a scan rate of 1 Hz. Top view images of the sample after the aggregate deposition were done employing Fei-NovaNanoSEM 650 high-resolution SEM with an acceleration voltage of 5 kV. Relative total and diffuse reflectance measurements were taken before the CIGS growth and after the full solar cell processing, the measurements were conducted with a Perkin-Elmer Lambda 950 UV-VIS-NIR

spectrophotometer tool. An XPS analysis was performed with an ESCALAB 250Xi system. For this analysis, a monochromated Al K<sub>α</sub> X-ray source was used with an energy of 1486.86 eV and the energy scale reference was the one of C 1s peak (284.60 eV). The flood gun was turned on to account for charge accumulation, the etch gun had an energy of 2000 eV and a current of 30 mA, the data was acquired at a pressure of approximately  $4 \times 10^{-7}$  mbar. The used fitting function was a convolution of a Gaussian and a Lorentzian with an L/G mix product of 0.3 with a modified Shirley background. The J-V curves were measured in illuminated and in dark conditions under a simulated and calibrated AM1.5 spectra in a homemade built-in system. EQE measurements were conducted using a QEX10 system, with a monochromatic light scanned through the wavelength values of 300 to 1100 nm, with a step of 10 nm.

### *Optical simulations*

Optical simulations of the fabricated solar cell stacks were conducted employing a 3D FDTD numerical method through the commercial software *Lumerical*.<sup>[34]</sup> Conversion tests were performed to minimize the computational requirements, while maintaining a high simulation accuracy. The surface roughness of the samples with nanoparticles was imported through AFM measurements. The refractive index and the extinction coefficient for the CIGS layer were taken from in-house spectroscopy ellipsometry measurements. The optical parameters for the ZnO:Al, i:ZnO and CdS layers were taken from<sup>[45]</sup>, the Al<sub>2</sub>O<sub>3</sub> from<sup>[46]</sup>, the Au material from<sup>[47]</sup> and the Mo layer from<sup>[48]</sup>.

### **Acknowledgments**

This work was funded in part by the Fundação para a Ciência e a Tecnologia (FCT) under Grants IF/00133/2015, PD/BD/142780/2018 and SFRH/BD/146776/2019. The authors also want to acknowledge the European Union's Horizon 2020 Research and Innovation Programme through the ARCIGS-M project under Grant 720887, the Special Research Fund (BOF) of

Hasselt University, the FCT through the project NovaCell (PTDC/CTM-CTM/28075/2017), and InovSolarCells (PTDC/FISMAC/29696/2017) co-funded by FCT and the ERDF through COMPETE2020.

Received: ((will be filled in by the editorial staff))

Revised: ((will be filled in by the editorial staff))

Published online: ((will be filled in by the editorial staff))

## References

- [1] J. F. Guillemoles, T. Kirchartz, D. Cahen, and U. Rau, *Nature Photonics* **2019**, 13, 501.
- [2] W. Shockley and H. J. Queisser, *J. Appl. Phys.* **1961**, 32, 510.
- [3] A. Duchatelet, E. Letty, S. Jaime-Ferrer, P. P. Grand, F. Mollica, and N. Naghavi, *Sol. Energy Mater. Sol. Cells* **2017**, 162, 114.
- [4] N. Naghavi, F. Mollica, J. Goffard, J. Posada, A. Duchatelet, M. Jubault, F. Donsanti, A. Cattoni, S. Collin, P. Grand, J. Greffet and D. Lincot, *Thin Solid Films* **2017**, 633, 55 – 60, Jul. **2017**.
- [5] O. Lundberg, M. Bodegård, J. Malmström, and L. Stolt, *Prog. Photovoltaics Res. Appl.* **2003**, 11, 77.
- [6] M. D. Heinemann, Florian Ruske, D. Greiner, Ahreum Jeong, Marin Rusu, Bernd Rech, Rutger Schlatmann, Christian A. Kaufmann, *Sol. Energy Mater. Sol. Cells* **2016**, 150, 76.
- [7] H. A. Atwater and A. Polman, *Nature Materials* **2010**, 9, 205.
- [8] M. Schmid, *Semiconductor Science and Technology* **2017**, 32, 043003.
- [9] P. Kowalczewski, A. Bozzola, M. Liscidini, and L. Claudio Andreani, *J. Appl. Phys.* **2014**, 115, 194504.
- [10] M. A. Green, *Prog. Photovoltaics Res. Appl.* **2002**, 10, 235.
- [11] S. Morawiec, M. J. Mendes, F. Priolo, and I. Crupi, *Materials Science in Semiconductor Processing* **2019**, 92, 10.
- [12] F. Enrichi, A. Quandt, and G. C. Righini, *Renewable and Sustainable Energy Reviews* **2018**, 82, 2433.
- [13] M. J. Mendes, S. Morawiec, F. Simone, F. Priolo, and I. Crupi, *Nanoscale* **2014**, 6, 4796.
- [14] S. Morawiec, M. J. Mendes, S. A. Filonovich, T. Mateus, S. Mirabella, H. Águas, I. Ferreira, F. Simone, E. Fortunato, R. Martins, F. Priolo and I. Crupi, *Opt. Express* **2014**, 22, A1059.
- [15] M. Schmid, J. Klaer, R. Klenk, M. Topič, and J. Krč, *Thin Solid Films* **2013**, 527, 308.

- [16] S. Pillai and M. A. Green, *Solar Energy Materials and Solar Cells* **2010**, 94, 1481.
- [17] S. Pillai, K. R. Catchpole, T. Trupke, and M. A. Green, *Journal of Applied Physics* **2007**, 101, 093105.
- [18] D. Derkacs, S. H. Lim, P. Matheu, W. Mar, and E. T. Yu, *Appl. Phys. Lett.* **2006**, 89, 093103.
- [19] K. Islam, A. Alnuaimi, E. Battal, A. K. Okay, and A. Nayfeh, *Sol. Energy* **2014**, 103, 263.
- [20] T. L. Temple and D. M. Bagnall, *Prog. Photovoltaics Res. Appl.* **2013**, 21, 600.
- [21] N. J. Halas, *Nano Lett.* **2010**, 10, 3816.
- [22] D. M. Schaadt, B. Feng, and E. T. Yu, *Appl. Phys. Lett.* **2005**, 86, 1.
- [23] K. L. Kelly, E. Coronado, L. L. Zhao, and G. C. Schatz, *J. Phys. Chem. B* **2003**, 107, 668.
- [24] M. Schmid, P. Andrae, and P. Manley, *Nanoscale Res. Lett.* **2014**, 9, 1.
- [25] G. Yin, P. Manley, and M. Schmid, *Sol. Energy* **2018**, 163, 443.
- [26] C. Eminian, F.-J. Haug, O. Cubero, X. Niquille, and C. Ballif, *Prog. Photovoltaics Res. Appl.* **2011**, 19, 260.
- [27] E. Moulin, J. Sukmanowski, M. Schulte, A. Gordijn, F. X. Royer, and H. Stiebig, *Thin Solid Films* **2008**, 516, 6813.
- [28] M. Nakamura, K. Yamaguchi, Y. Kimoto, Y. Yasaki, T. Kato, and H. Sugimoto, *IEEE J. Photovoltaics* **2019**, 9, 1863.
- [29] L. Stamford and A. Azapagic, *Sci. Total Environ.* **2019**, 688, 1092.
- [30] G. Yin, A. Steigert, P. Andrae, M. Goebelt, M. Latzel, P. Manley, I. Lauermann, S. Christiansen and M. Schmid, *Appl. Surf. Sci.* **2015**, 355, 800.
- [31] T. S. Lopes, J. M. V. Cunha, S. Bose, J. R. S. Barbosa, J. Borme, O. Donzel-Gargand, C. Rocha, R. Silva, A. Hultqvist, W.-C. Chaen, A. G. Silva, M. Edoff, P. A. Fernandes, P. M. P. Salomé, *IEEE J. Photovoltaics* **2019**, 9, 1421.
- [32] P. M. P. Salomé, B. Vermang, R. Ribeiro-Andrade, J. P. Teixeira, J. M. V. Cunha, M. J. Mendes, S. Haque, J. Borme, H. Águas, E. Fortunato, R. Martins, J. C. González, J. P. Leitão, P. A. Fernandes, M. Edoff, S. Sadewasser, *Adv. Mater. Interfaces* **2018**, 5, 1701101.
- [33] T. A. Green, *Gold Bulletin* **2014**, 47, 205.
- [34] High-Performance Photonic Simulation Software - Lumerical,

- <https://www.lumerical.com/>, accessed: May 2020.
- [35] A. Čampa, J. Krč, J. Malmström, M. Edoff, F. Smole, and M. Topič, *Thin Solid Films* **2007**, 515, 5968.
- [36] N. Dahan, Z. Jehl, T. Hildebrandt, J. -J. Greffet, J. -F. Guillemoles, D. Lincot and N. Naghavi *J. Appl. Phys.* **2012**, 112, 094902.
- [37] S. S. Hegedus and W. N. Shafarman, *Prog. Photovoltaics Res. Appl.* **2004**, 12, 155.
- [38] M. K. Bahl, R. L. Watson, and K. J. Irgolic, *J. Chem. Phys.* **1980**, 72, 4069.
- [39] P. M. P. Salomé, P. A. Fernandes, J. P. Leitão, M. G. Sousa, J. P. Teixeira, and A. F. Da Cunha, *J. Mater. Sci.* **2014**, 49, 7425.
- [40] K. W. Böer, *Handbook of the physics of thin-film solar cells*, Springer, Berlin, Germany **2013**.
- [41] B. V. Enüstün and J. Turkevich, *J. Am. Chem. Soc.* **1963**, 85, 3317.
- [42] L. Scarabelli, M. Grzelczak, and L. M. Liz-Marzán, *Chem. Mater.* **2013**, 25, 4232.
- [43] S. Bose, J. M. V. Cunha, S. Suresh, J. De Wild, T. S. Lopes, J. R. S. Barbosa, R. Silva, J. Borme, P. A. Fernandes, B. Vermang and P. M. P. Salomé, *Sol. RRL* **2018**, 2, 1800212.
- [44] S. Garud, N. Gampa, T. G. Allen, R. Kotipalli, D. Flandre, M. Batuk, J. Hadermann, M. Meuris, J. Poortmans, A. Smets and B. Vermang, *Phys. Status Solidi Appl. Mater. Sci.* **2018**, 215, 1.
- [45] R. Carron, E. Avancini, T. Feurer, B. Bissig, P. A. Losio, R. Figi, C. Schreiner, M. Bürki, E. Bourgeois, Z. Remes, M. Nesladek, S. Buecheler, A. N. Tiwari, *Sci. Technol. Adv. Mater.* **2018**, 19, 396.
- [46] E. D. Palik, *Handbook of Optical Constants of Solids, Five-Volume Set*. Elsevier Science, USA **1997**.
- [47] P. B. Johnson and R. W. Christy, "Optical constants of the noble metals," *Phys. Rev. B* **1972**, 6, 4370.
- [48] W. S. M. Werner, K. Glantschnig, and C. Ambrosch-Draxl, *J. Phys. Chem. Ref. Data* **2009**, 38, 1013.

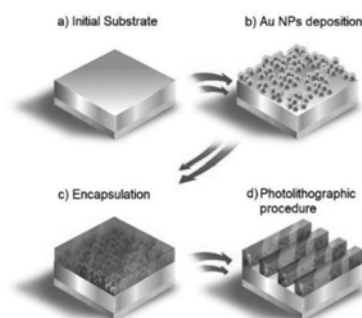


**Figure 1.** Schematic illustration of the novel rear structure fabrication process. a) Initial soda-lime glass + Mo substrate; b) Au NPs deposition on top of the Mo layer; c) Au NPs encapsulation with a 25 nm  $\text{Al}_2\text{O}_3$  layer; and d) Photolithographic procedure to create a line pattern.

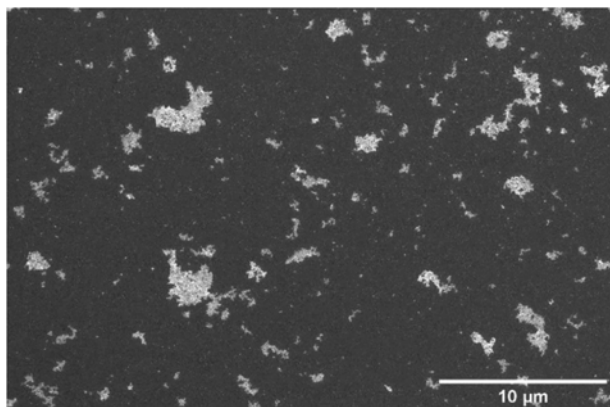


**Figure 2.** SEM top view image of sample NPep after the Au NP deposition. Through the analysis of several SEM images, an average surface coverage of  $(4.6 \pm 0.7) \%$  was obtained.

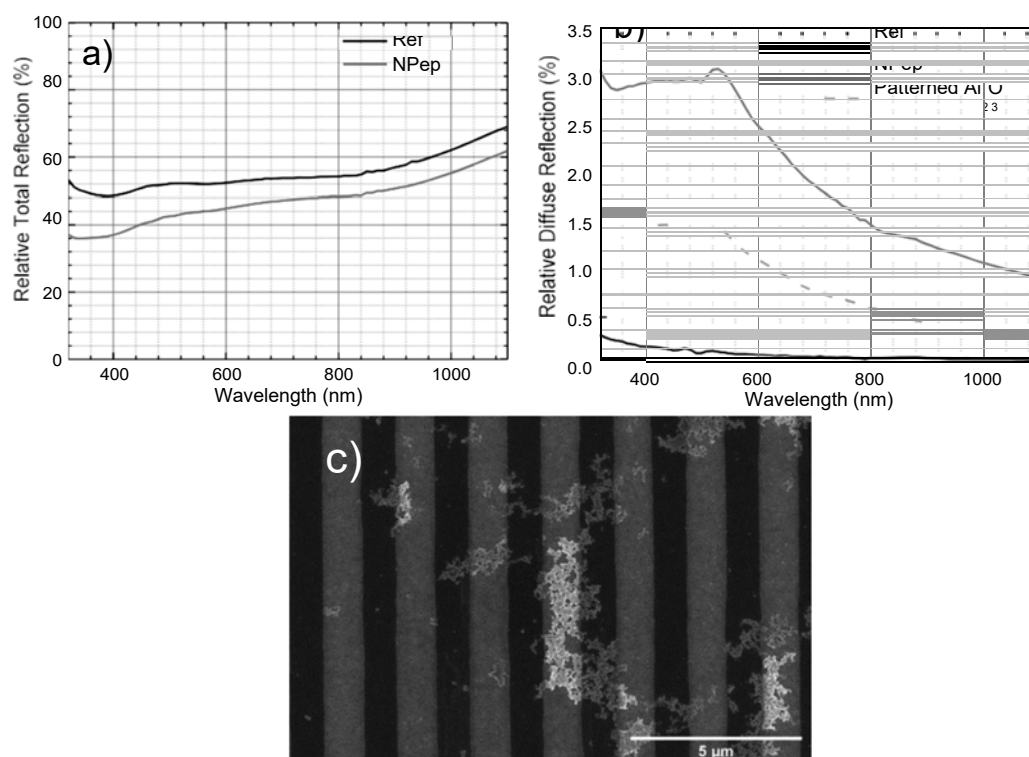


**Figure 3.** a) Relative total reflection of Ref and NPep samples for radiation wavelength values between 300 and 1100 nm; b) Relative diffuse reflection of sample Ref, NPep and a patterned Al<sub>2</sub>O<sub>3</sub> sample for the same spectral region. With the implementation of the novel architecture (sample NPep), we observe a decrease in the total reflection. However, an increase of the diffuse reflection that would allow for an enhancement of the optical path length inside the absorber layer is verified; and c) SEM top view image of sample NPep, we observe the remaining Au nanoparticles/aggregates inside the line contacts (dark lines) after the lithographic step.





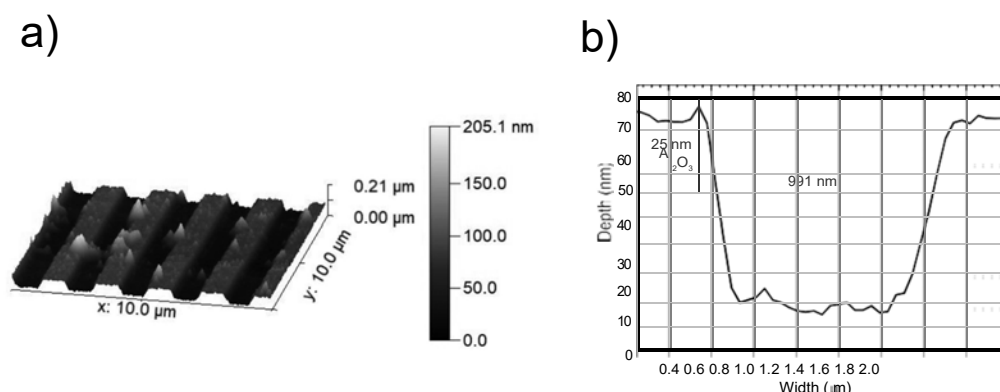


**Figure 4.** a) AFM 3D image of Sample NPep; and b) AFM cross-section plot of sample NPep. The cross-section image shows the height of the  $\text{Al}_2\text{O}_3$  passivation layer and the consequent etch on Mo. Moreover, values of the line contact width were extracted on the top of the Mo layer where the  $\text{Al}_2\text{O}_3$  should be etched away considering its thickness, as it is represented by the red dot line. The line contact width value presented, corresponds to the average value.

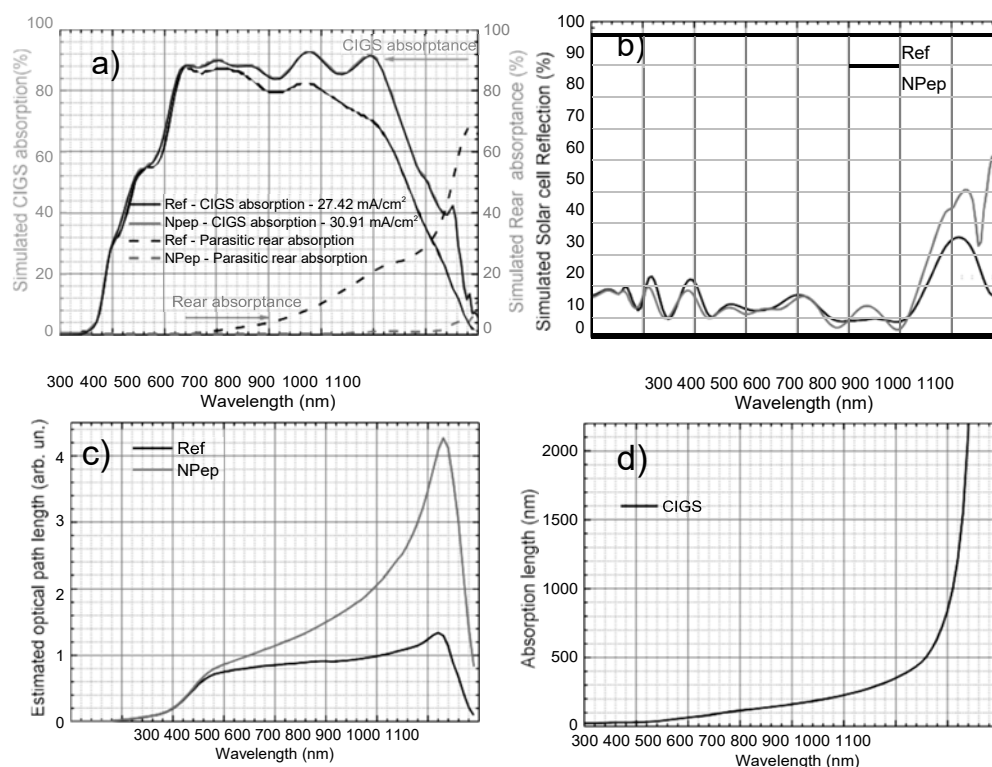


**Figure 5.** a) Simulated absorption in the CIGS layer (solid lines) and rear parasitic absorption

55 (dashed lines) of the Ref and NPep devices, with the simulated  $J_{sc}$  being shown; b) Simulated  
56 solar cells total reflectance of the Ref and NPep devices. With the implementation of the novel  
57 architecture (NPep device), it is possible to observe a broadband increase of the light absorbed

in the CIGS layer. Furthermore, an improvement on the anti-reflection properties of the solar cell is verified through the reduced reflection of the NPep device over the Ref device; c) Calculated optical path length for the Ref and NPep devices; d) Calculated absorption length of CIGS. An optical path length higher than 1, for wavelength values above 900 nm, is already verified for the Ref device, suggesting that some light management occurs in this device. With the implementation of the novel architecture, an increase of the optical path length of approximately 4 times the nominal thickness of the absorber layer is verified at a wavelength value of 1030 nm.

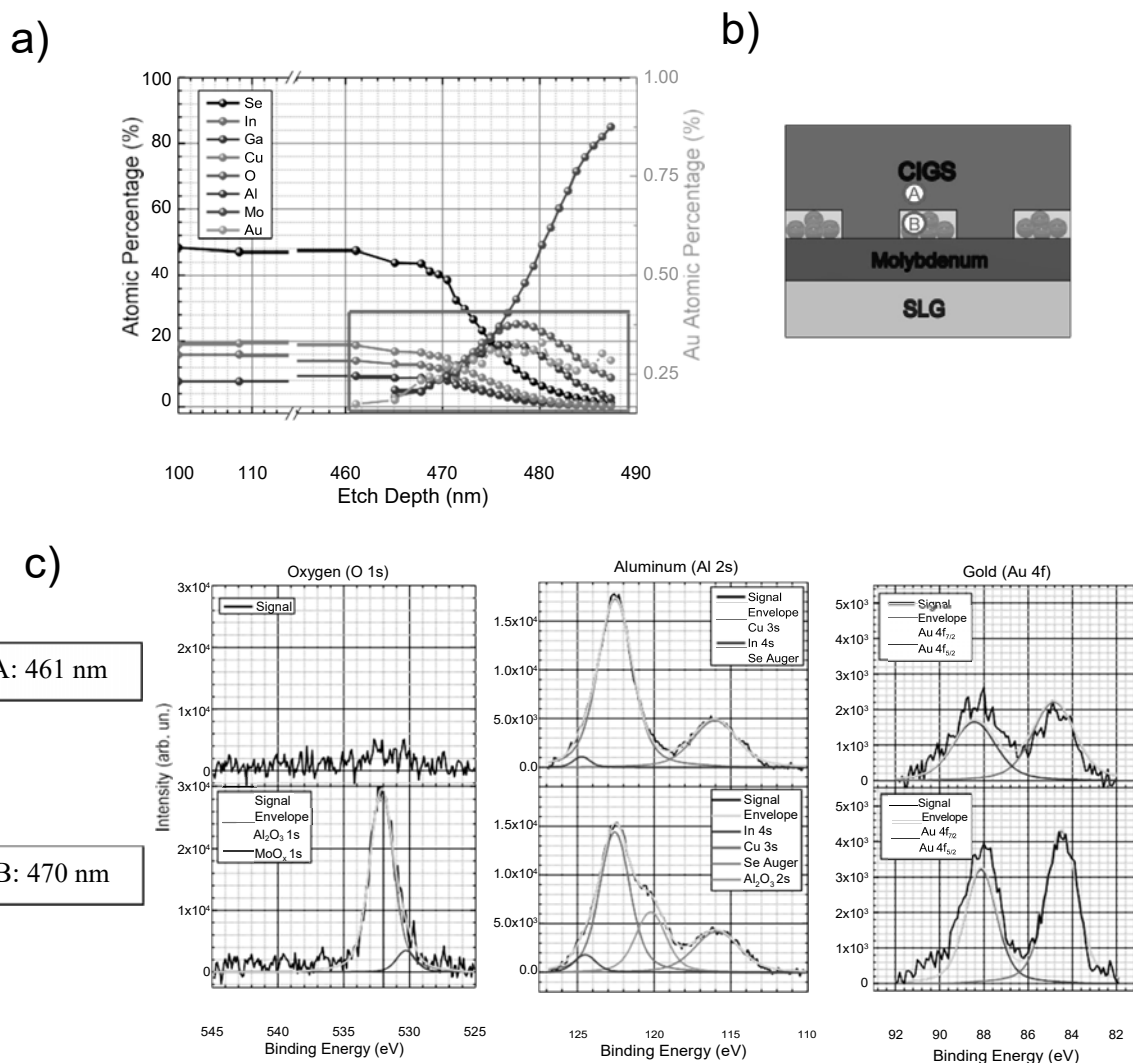


**Figure 6** a) Depth profile from the middle of the CIGS until the back contact; b) Schematic of the studied sample, with an illustrative representation of two etching depths. c) XPS spectra of O 1s, Al 2s and Au 4f at representative etching depths. The Au 4f peaks can start being detected at point A, while at this depth the O 1s and the Al 2s peaks are not detected. At a deeper site

54 (point B) the O 1s and the Al 2s peaks can be detected at 532.1 eV and 120.2 eV, respectively.  
55  
56 The Au 4f peak was fitted with an intensity ratio of 3:4 and a spin orbit splitting constraint of  
57 approximately 3.70 eV.

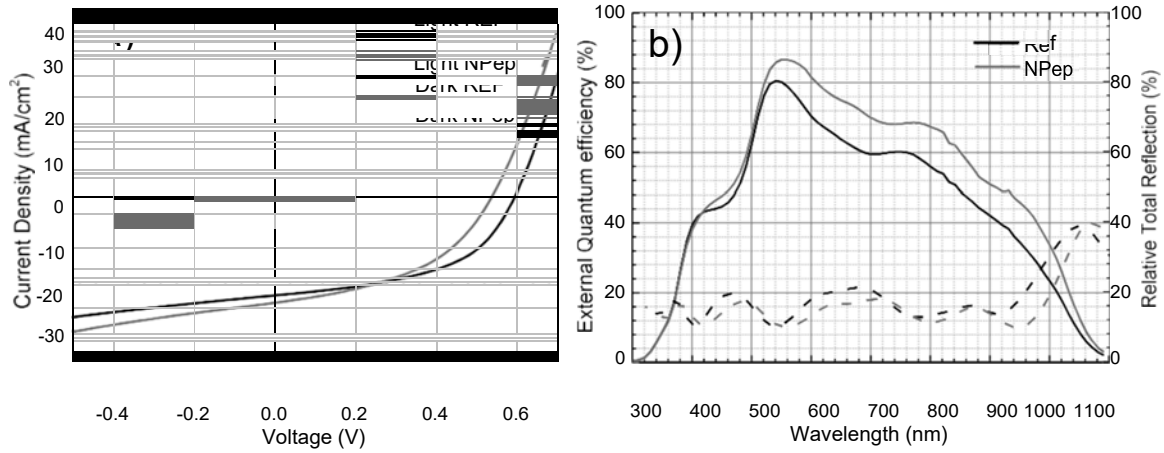


**Figure 7.** a) Illuminated (solid lines) and dark (dashed lines) J-V curves of representative Ref and NPep solar cells. Evidences of shunting are verified for both devices, as suggested through the steep slopes for negative voltages; b) Representative EQE (solid lines) and relative total reflection (dashed lines) curves for the Ref and NPep devices. With the implementation of the novel architecture (NPep device), it is possible to observe a broadband increase of the EQE. Furthermore, an improvement in the anti-reflection properties of the solar cell is verified through the reduced reflection of the NPep device over the Ref device.

**Table 1.** Averages with standard variation values of J V parameters,  $V_{oc}$  and  $FF$ , and the  $J_{sc}$  parameter calculated from the EQE spectrum, for Ref and NPep devices. The values corresponding to the solar cells with the highest power conversion efficiency ( $Eff$ ) are also presented in ().

Solar Cell	$V_{oc}$ [mV]	$J_{sc}$ [mA/cm <sup>2</sup> ]	$FF$ [%]	$Eff$ [%]
Ref	$580 \pm 10$ (596)	$21.24 \pm 0.84$ (22.46)	$51.2 \pm 5.2$ (60.5)	$6.32 \pm 0.83$ (8.10)
NPep	$521 \pm 18$ (550)	$24.93 \pm 0.60$ (25.90)	$44.6 \pm 5.7$ (57.0)	$5.83 \pm 1.03$ (8.11)



In this work, the study and integration of a novel nanostructure based on Au nanoparticles aggregates on the back contact of an ultra-thin Cu(In,Ga)Se<sub>2</sub> solar cell is developed. The nanoparticles are effectively encapsulated with a dielectric matrix providing a broadband external quantum efficiency enhancement that translates to a 17.4 % improvement of the short circuit current over a reference device.

### Photovoltaics

António Oliveira, Jessica de Wild, Kevin Oliveira\*, Beatriz Valença, Jennifer Teixeira\*, Joana Guerreiro, Sara Abalde-Cela, Tomás Lopes, Rodrigo Ribeiro, José Cunha, Marco Curado, Margarida Monteiro, Ana Gomes Silva, André Violas, Marta Prado, Paulo Fernandes, Bart Vermang, Pedro Salomé

### Encapsulation of Nanostructures in a Dielectric Matrix providing Optical Enhancement in Ultra-thin Solar cells

